

Simultaneous Activation–Exfoliation–Reassembly to Form Layered Carbon with Hierarchical Pores

Wei Li Ong,^[a] Judith Hui Min Wong,^[a] Serene Wen Ling Ng,^[a] Hui Ru Tan,^[c] Yee Fun Lim,^[c] and Ghim Wei Ho*^[a, b, c]

Currently, the production of hierarchical 2D layered carbon is mostly limited by low yields, laborious processing, and the high tendency for reaggregation. Hence, it is still a challenge to attain stable porous carbon structures with a well-preserved layered structure and hierarchical pores. Here, we demonstrate a facile and simultaneous activation–exfoliation–reassembly technique to perform structural modification and pore tailoring of carbonaceous matrices conveniently. Various pore creations

can be realized concurrently from in-plane micro-/mesopores by chemical activation, expansion of intersheet mesopores, and interconnectivity of the layered structure to form 3D macropores. Finally, a proof-of-concept demonstration of the combination of hierarchical macro-/micro-/mesoporous layered carbon structure and TiO₂ nanosheets shows promising adsorption and catalytic properties.

Introduction

Carbon layered materials have gained much attention recently because of the emergence of new properties when a few-layer thick sheets are constructed that behave vastly different from the bulk multilayered carbon.^[1] Carbon layered materials, specifically graphene and its derivatives, have been studied extensively and developed for various potential applications that include their use as catalysts, sorbents, energy storage, and energy conversion.^[2–4] Essentially, 2D layered materials constitute a good alternative to a particulate/bulk structure as they possess a host of attributes, which include a shortened charge transport dimension, large surface area, abundant exposed sites, and optimized contact interfaces.^[5] At the same time, the stability of the layered structures along with their exceptional topotactic interactions and reactivity offer intriguing opportunities for manipulation and hybridization towards a desirable functional nanocomposite.

The in-plane chemical bonds of carbon are stronger than the out-of-plane bonds, which allow it to be exfoliated into 2D layered structures. If we take advantage of the intrinsic 2D configuration of carbon, one of the most common methods to

fabricate the layered sheets is by the mechanical exfoliation of bulk graphite to cleave, delaminate, and split apart the crystal layers.^[6] Liquid exfoliation has also been achieved in various surfactant and intercalator media followed by long-duration ultrasonication.^[7] Besides, bottom-up approaches, that is, vapor–solid and chemical vapor deposition (CVD) methods, have also been demonstrated to produce few-layer carbon materials mostly limited on substrates.^[8] Additionally, graphene/carbon layered structures show a high tendency to reaggregate or self-stack during the processing steps, which results in a substantial loss of the active surface area and hence leads to a decreased physicochemical performance. Consequently, it is still a challenge to fabricate stable/robust carbon layered structures with well-preserved hierarchical pores on a large scale.

Herein we demonstrate a cost- and process-effective method to simultaneously activate–exfoliate–reassemble carbon nanospheres into thin-layered hierarchical porous structures. Compared to other preparation routes, the activation–exfoliation–reassembly approach fulfills the formation of thin-layered planar sheets and hierarchical pores with large specific surface areas conveniently. As such, the proposed technique is attractive because of its easy procedure, mild conditions, high reproducibility, and controllability. Other than the formation of primary in-plane micro-/mesopores introduced by chemical activation, the expansion of interlayer galleries between the lamellar structures leads to spontaneous exfoliation that then creates an additional level of hierarchy mesopores. Finally, the congruent exfoliation–reassembly of the carbon layered structure affords a 3D interconnected macroporous framework. A proof-of-concept demonstration shows that the constructed hierarchical porous carbon structure with well-assembled TiO₂ nanosheets (NSs) leads to the efficient transport of the reactant throughout the carbonaceous matrix, which leads to an enhanced adsorption and catalytic performance.

[a] Dr. W. L. Ong, J. H. M. Wong, S. W. L. Ng, Prof. G. W. Ho
Department of Electrical and Computer Engineering
National University of Singapore
4 Engineering Drive 3, Singapore 117583 (Singapore)
E-mail: elehgw@nus.edu.sg

[b] Prof. G. W. Ho
Engineering Science Programme
National University of Singapore
9 Engineering Drive 1, Singapore 117575 (Singapore)

[c] H. R. Tan, Dr. Y. F. Lim, Prof. G. W. Ho
Institute of Materials Research and Engineering
A*STAR (Agency for Science, Technology and Research),
3 Research Link, Singapore 117602 (Singapore)

Supporting information for this article can be found under:
<https://doi.org/10.1002/cctc.201700137>.

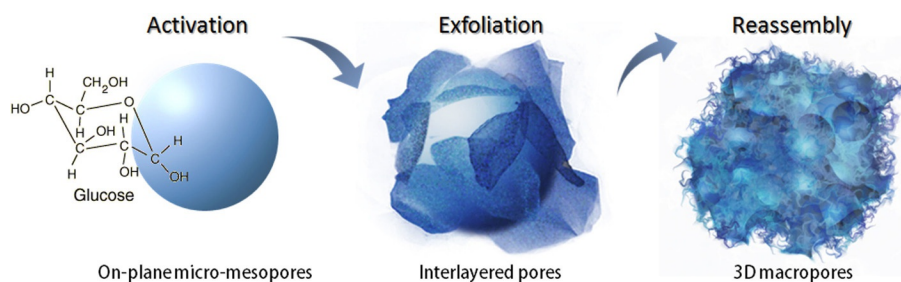
Results and Discussion

Carbon spheres (CSs) were obtained from a simple hydrothermal treatment of glucose and subsequently subjected to KOH treatment with a CS/KOH mass ratios of 1:2 (AC-1), 1:4 (AC-2), and 1:6 (AC-3), during which the CSs undergo a simultaneous process of activation, exfoliation, and reassembly, which results in a transformation of the CSs into a 3D interconnected macro-porous framework as illustrated in Scheme 1.

The pristine CSs have a smooth surface and uniform diameter of approximately 250 nm, and no visible pores were observed in the corresponding TEM images (Figure S1). When these nano-sized CSs were subjected to KOH activation treatment, the exfoliation and peeling of the outer layers were observed (Figure 1a and b). With increased amounts of KOH, the CSs were disintegrated by the exfoliation process and monolithic fragments with irregular shapes and “Swiss-cheese”-like macropores^[9] of varying sizes were observed (Figure 1c). The monolith is formed by a reassembly of the carbon sheets into a 3D macro-/micro-/mesoporous carbonaceous matrix (Figure 1d). The textural characteristics of these porous carbon structures were investigated by analyzing the BET measurements. The N₂ adsorption–desorption isotherm measured at 77 K is shown in Figure 1e, and the corresponding pore size distribution is shown in Figure 1f. The microstructural properties, which include the specific surface area, pore volume, and average pore diameter, are summarized in Table 1. The isotherms of the pristine CSs can be identified as Type III according to the IUPAC classification. The adsorbed amount was very low and close to zero at relatively low pressures, which suggests the low porosity of the solid pristine CSs. The total pore and micropore volume of the CSs were 0.03187 and 0.0119 cm³ g⁻¹, respectively, which are in agreement with the predicted values for CSs without pore structures. After KOH treatment, AC-1 and AC-2 exhibited Type II isotherms and AC-3 exhibited a Type I isotherm. From the isotherms, AC-1 has the lowest rate of adsorption at low pressures, which indicates that it has the lowest number of micropores amongst the AC samples. In comparison, a rapid saturation at low pressures is observed in AC-2 and AC-3, which indicates the existence of large amounts of micropores.^[10] AC-1 has a surface area of 1115 m² g⁻¹, which is more than 100 times larger than that of pristine CSs (10.33 m² g⁻¹), and this can be attributed to the presence of mesopores and micropores ($V_t=0.898$ cm³ g⁻¹, $V_{\text{micro}}=0.714$ cm³ g⁻¹). The BET surface area of AC-2 and AC-3 is

1533 m² g⁻¹ ($V_t=0.796$ cm³ g⁻¹, $V_{\text{micro}}=0.681$ cm³ g⁻¹) and 2107 m² g⁻¹ ($V_t=0.945$ cm³ g⁻¹, $V_{\text{micro}}=0.877$ cm³ g⁻¹), respectively. The high surface area observed for AC-3 can be attributed to the formation of large amounts of pores because of the vigorous etching at a high concentration of KOH. In addition to the BET surface area analysis, the quenched solid state density functional theory (QSDFT) method was also used to analyze the distribution of the micro- and mesopores. The AC samples exhibit a multimodal distribution in both the micropore and mesopore domains (Figure 1f). The micropores of AC-2 have a peak pore size of approximately 0.39 nm, and with increasing amounts of KOH, a larger pore size with a wider pore size distribution was observed because of the pore-widening effect caused by KOH inside the existing pores.^[11] This effect is observed in the micropores of AC-3, which has a peak pore size of approximately 0.51 nm. These results indicate that KOH activation of CSs can produce carbonaceous structures with a highly developed porosity, and also significant increases in surface area and pore volume. The surface properties of the carbon structures before and after KOH activation were analyzed by using FTIR spectroscopy (Figure 1g). The broad peak at $\tilde{\nu}=3400$ cm⁻¹ is associated with the –OH stretching vibration of hydroxyl functional groups, and the intensity of the peak decreases with the increase of the amount of KOH used during activation. This could be because of dehydration that occurs during the activation process. The peak at $\tilde{\nu}=1160$ cm⁻¹ corresponds to the C–OH bending vibrations.^[12,13] The band at $\tilde{\nu}=1640$ cm⁻¹ is assigned to the C=O stretch of a nonaromatic carboxylic moiety, which might be derived from the partial dehydrogenation of glucose during the hydrothermal reaction. A weak vibration was observed at $\tilde{\nu}=1380$ cm⁻¹, which is consistent with the presence of O=C–O groups, and the intensity of this band decreases with the increase of the amount of KOH activation.

The morphological features were further characterized by using TEM (Figure 2). No visible pores were observed in the TEM images of the pristine CSs (Figure S1). After KOH activation, the exfoliation and peeling of the outer layers of AC-2 were observed clearly (Figure 2a) and the spherical structure appears porous. The high-magnification TEM image of the selected area of Figure 2a reveals the presence of a few-layer porous nanosheets on the exterior of the spherical structure (Figure 2b) and the high-resolution transmission electron microscopy (HRTEM) image suggests the presence of graphitic carbon structure. If more KOH was used (AC-3), a porous net-



Scheme 1. Schematic diagram that illustrates the morphological evolution of CSs through the activation, exfoliation, and reassembly of thin carbon planar sheets.

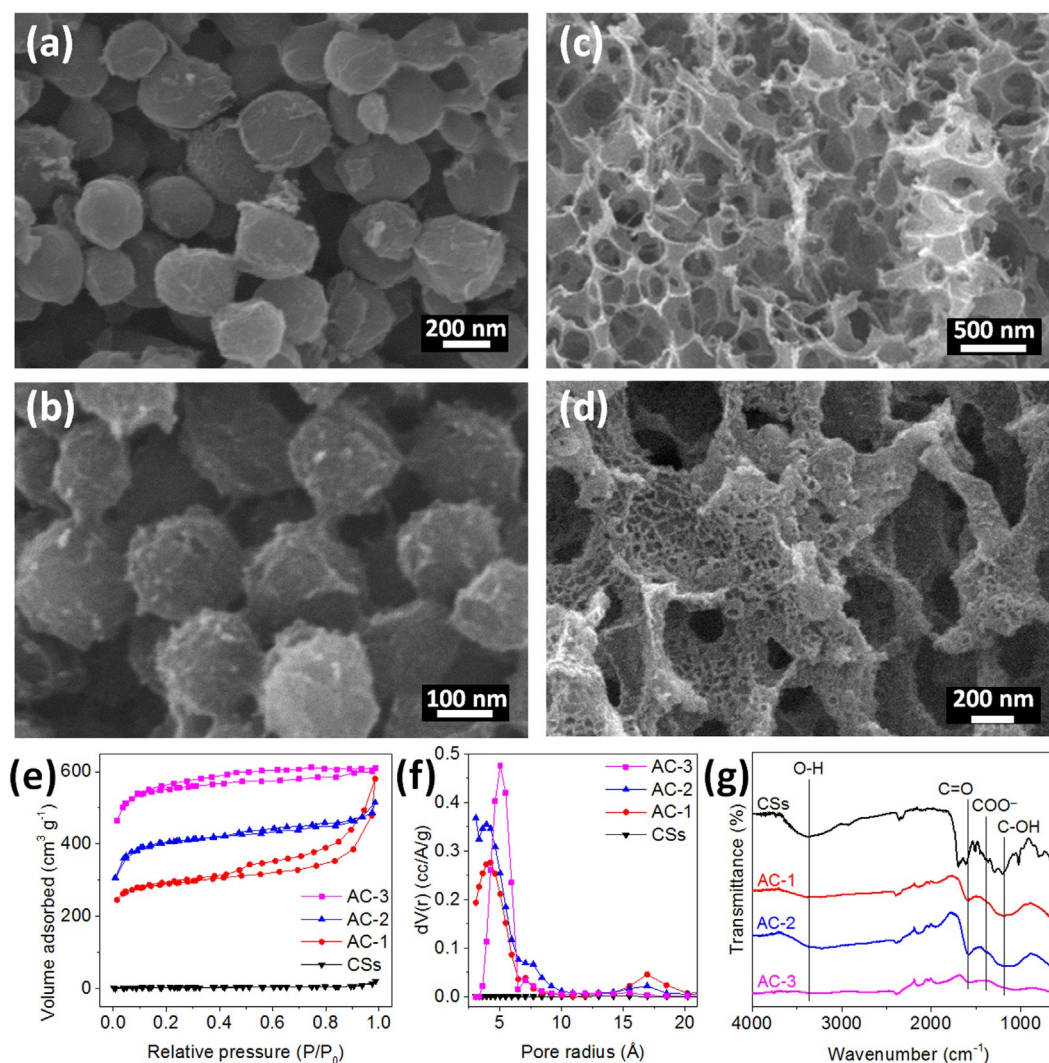


Figure 1. Low- and high-magnification SEM images of a, b) AC-2 and c, d) AC-3 that depict the exfoliation and reassembly of thin carbon planar sheets upon KOH activation treatment. e) N₂ adsorption–desorption isotherms measured at 77 K, f) the corresponding pore size distributions obtained by using QSDFT, and g) FTIR spectra that detail the surface properties of CSs and AC.

Sample	S_{micro} [m ² g ⁻¹]	$S_{\text{BET}}^{[a]}$ [m ² g ⁻¹]	$V_{\text{micro}}^{[b]}$ [cm ³ g ⁻¹]	V_{meso} [cm ³ g ⁻¹]	$V_t^{[c]}$ [cm ³ g ⁻¹]	Ratio _{micro} [%]	Average pore size [nm]
CSs	6.343	10.33	0.012	0.019	0.032	40.63	6.91
AC-1	1065	1115	0.714	0.184	0.898	79.51	1.61
AC-2	1450	1533	0.681	0.116	0.796	85.43	1.28
AC-3	1657	2107	0.877	0.067	0.945	92.91	0.89
TiO ₂ -AC	162.1	163.9	0.146	0.011	0.156	92.95	1.93
TiO ₂ NSs	0	94.93	0	0.295	0.295	0	17.51
A-TiO ₂	0	6.35	0	0.036	0.036	0	11.59

[a] The surface area was calculated using the BET method at $P/P_0 = 0.01-0.1$. [b] Evaluated by the QSDFT method. [c] Total pore volume at $P/P_0 = 0.99$.

work of thin carbon sheets was observed (Figure 2d) and the marked area in Figure 2d actually consists of sparsely distributed thin carbon nanosheets (Figure 2e). These nanosheets are filled with micropores and mesopores as indicated by using SEM (Figure 1d) and QSDFT analysis (Figure 1f). Similarly, the ordered arrangement of the lattice fringes displayed in Fig-

ure 2f also suggests the presence of graphitic carbon. The XRD pattern of AC-3 (Figure S2) also reveals the presence of the typical (002) and (100) peaks from graphitic carbon.

During the activation process, the CSs react with KOH and undergo etching through a series of chemical reactions listed below [Eqs. (1)–(8)]:^[14]

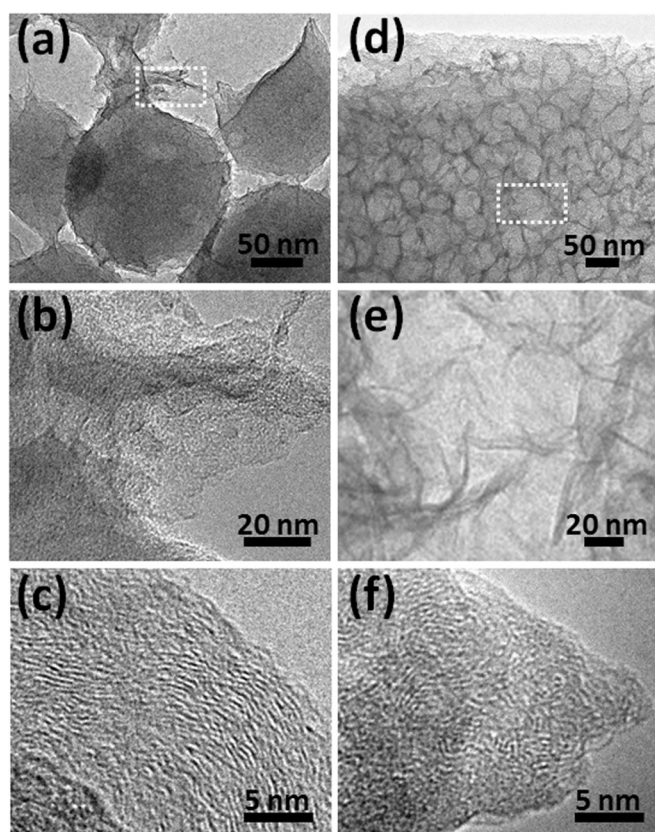
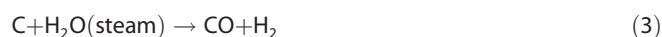
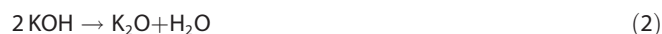


Figure 2. TEM and HRTEM images of a–c) AC-2 and d–f) AC-3.



In Equations (1), (3), (7), and (8), carbon undergoes etching to result in the formation of exfoliated sheets and also primary in-plane micro- and mesopores. The exfoliation could be attributed to the infusion of KOH into the CSs, which breaks down the structural integrity and causes the peeling of the sheets.^[15] It is also possible that the metallic K penetrates into the carbon lattices to cause an expansion of the lattices by the intercalated metallic K, and subsequently, the intercalated K is removed from the carbon matrix.^[16] This expansion of the inter-layer galleries between the lamellar structures leads to spontaneous exfoliation, which in turn creates an additional level of hierarchy mesopores. If the amount of KOH is increased, vigorous etching of the core and the surface of CSs occurs simultaneously, and the interconnections between the CSs remain to result in a morphological transformation of the spheres into nanosheets that are readily cross-linked because of the polycondensation effect.^[15,17] This congruent exfoliation–reassembly of the carbon layered structure produces a 3D interconnected macroporous framework.

As a demonstration of the functional properties of the porous carbon structures, the adsorption performance in both methyl orange (MO) aqueous solutions and volatile organic compound (VOC) vapors was investigated. The MO adsorption properties of the CSs were enhanced significantly after activation (Figure 3a). The pristine CSs did not adsorb any MO at all (not shown), whereas AC-2 performed the best and managed to adsorb the MO molecules fully in 90 min. AC-1 did not perform as well and adsorbed only 90% of MO after 120 min, whereas AC-3 achieved complete adsorption but only after

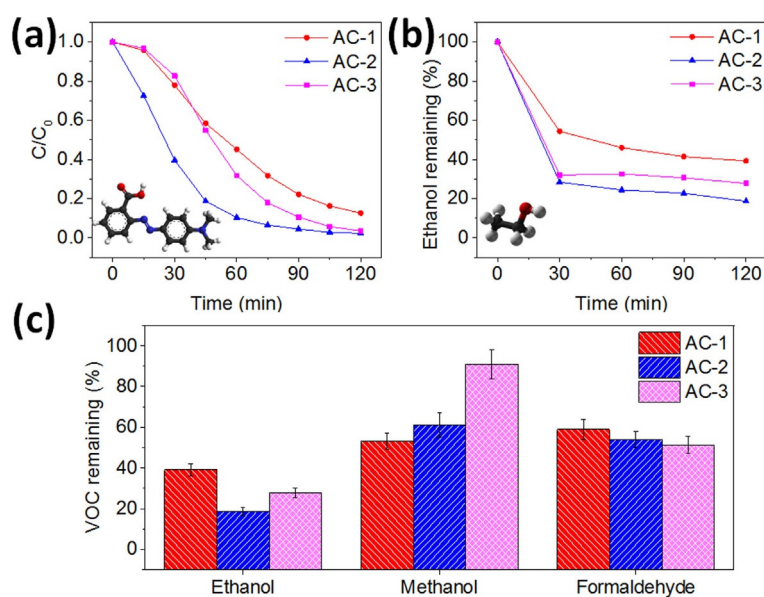


Figure 3. Adsorption kinetics over time of a) MO, b) ethanol, and c) the adsorption of various VOCs in the presence of AC.

120 min. A similar trend was also observed in the adsorption of ethanol vapor (Figure 3b). AC-2 exhibited the fastest rate of adsorption followed by AC-3 then AC-1. AC-2 was able to remove 80% of the ethanol in 120 min. The adsorption of the three VOCs investigated is summarized in Figure 3c. In both methanol and formaldehyde, AC-2 was the second-best-performing sample. This could be because the individual AC samples possess different affinities towards different VOC molecules.

TiO₂ NSs were then grown hydrothermally on AC-2 to form a TiO₂-AC composite material as a proof-of-concept demonstration. From the SEM image (Figure 4a), each of the AC nanospheres was observed to be covered uniformly by well-assembled TiO₂ NSs to form hierarchical flower-like nanostructures. The TEM image (Figure 4b) and energy-dispersive X-ray spectroscopy (EDX) elemental maps (Figure 4c) reveal the core-shell structure of the composite in which the AC core is encompassed fully by a radial assembly of 2D TiO₂ NSs on the outer surface. The fairly transparent appearance of the TiO₂ NSs in the TEM image shown in Figure 4d suggests the ultrathin nature of the 2D sheets. These 2D NSs possess both physical and chemical advantages over nanoparticles such as a high surface area to volume ratio, extensive interfacial contact area, and easily accessible reaction sites. The HRTEM image of the TiO₂ NSs in Figure 4e shows clear lattice fringes, which indicates the good crystallinity of the TiO₂ NSs, and the lattice spacing of 0.35 nm corresponds to the (101) plane of anatase TiO₂. The XRD diffraction pattern obtained from the TiO₂-AC composite is the same as that of the pristine TiO₂ NSs (Figure 4f). The peaks at $2\theta = 25.34, 37.91, 48.10, 54.14, 55.17, 62.73, 68.88, 70.29, \text{ and } 75.13^\circ$ can be indexed to the (101), (004), (200), (105), (211), (204), (116), (220), and (215) crystal planes of anatase TiO₂ (JCPDS card no. 21-1272), which indi-

cates that the TiO₂ NSs in the TiO₂-AC composite are also in the anatase phase.

BET measurements were performed on TiO₂-AC, and the corresponding isotherm and pore size distributions are plotted in Figure S3. The microstructural details are listed in Table 1. The structural properties of commercial anatase TiO₂ (A-TiO₂) nanoparticles and pristine TiO₂ NSs were included for comparison. The TiO₂-AC composite exhibits a Type I isotherm, which suggests the presence of large amounts of micropores because of the AC-2 at the core of the hierarchical structure. The composite has a surface area of 162.1 m²g⁻¹, which is higher than that of both A-TiO₂ (6.35 m²g⁻¹) and TiO₂ NSs (94.93 m²g⁻¹) because of the presence of AC-2, which suggests the excellent adsorption capacity of TiO₂-AC. However, the surface area of TiO₂-AC is lower than that of AC-2 possibly because of a partial coverage or blockage of the pores during the synthesis of TiO₂.^[18] The UV/Vis absorption spectra of the various samples are shown in Figure S4. The TiO₂-AC composite exhibited a marked increase in absorption in the visible region without any observable shift in the band gap. This indicates that the presence of a carbon core enhances the absorption of visible wavelengths greatly, which can aid in the enhancement of photocatalytic activity through the generation of more electron-hole pairs under UV/Vis illumination.

The samples were then tested in the photodegradation of MO (Figure 5), which is akin to demonstrating its capability in wastewater treatment. When the TiO₂-AC composite is illuminated by solar irradiation, the photogenerated electrons will react with dissolved oxygen molecules to form oxygen peroxide radicals O₂⁻, whereas the photogenerated holes react with H₂O to produce hydroxyl radicals OH[•] (Figure S5). These reactive oxidizing radicals will then mineralize the organic pollutants into CO₂, H₂O, and other mineralization products.^[19,20]

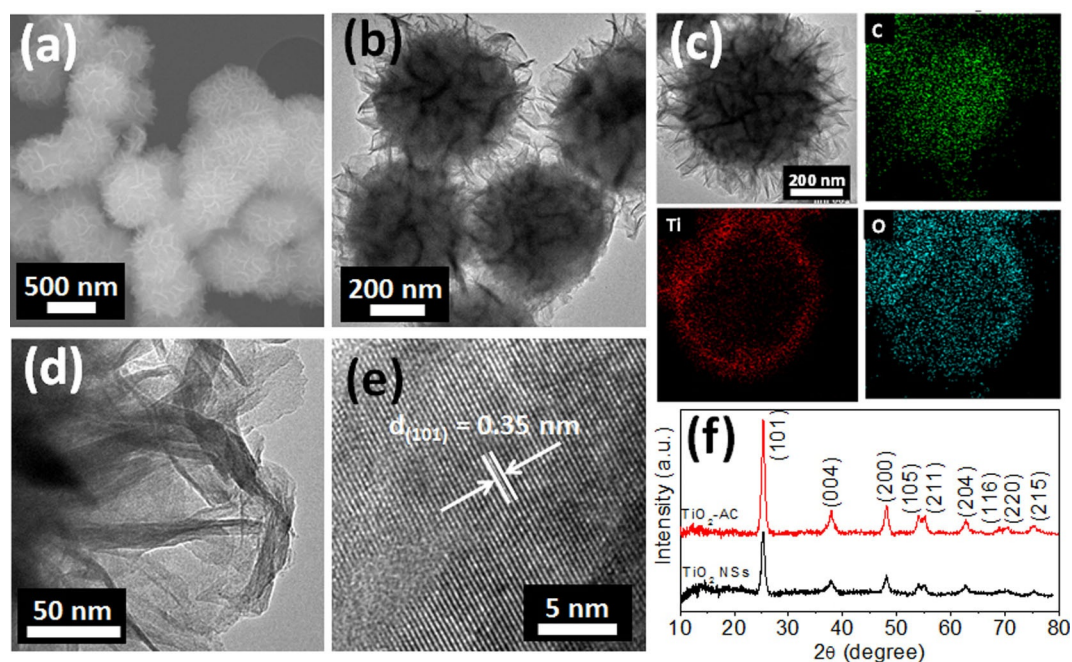


Figure 4. a) SEM and b) TEM images and c) elemental maps of the TiO₂-AC composite. d) High-magnification TEM and e) HRTEM images of TiO₂ NSs in the TiO₂-AC composite. f) XRD pattern of pristine TiO₂ NSs and the TiO₂-AC composite.

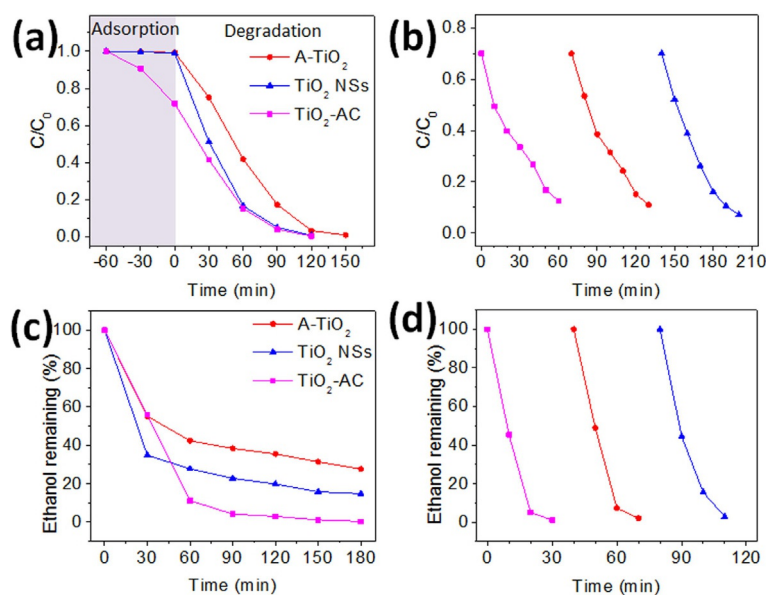


Figure 5. Degradation kinetics over time of a) MO and c) ethanol photodegradation in the presence of A-TiO₂, TiO₂ NSs, and TiO₂-AC. Repeated cycling in the photocatalytic degradation of b) MO and d) ethanol in the presence of TiO₂-AC composite.

Before illumination, the mixture was stirred magnetically in the dark for 60 min to attain an adsorption–desorption equilibrium between the composite material and the MO solution. A significant amount of MO was adsorbed by the TiO₂-AC composite in the dark, whereas little or no adsorption was observed for A-TiO₂ and TiO₂ NSs (Figure 5a). This is because of the presence of AC, which is a very strong adsorbent, in the core of the composite material. Upon illumination, the TiO₂-AC composite performed the best and was able to degrade MO completely in 120 min. This enhancement in the degradation performance can be attributed to the high surface area of the TiO₂ NSs and the high adsorption capability of AC. The adsorption of MO by the AC core helps to concentrate the MO molecules for faster degradation by TiO₂. The photodegradation activity was further analyzed by studying the pseudo-first-order kinetics of the various photocatalysts (Figure S6), and the rate constants k are summarized in Table S1. A-TiO₂ has the lowest k of 0.0317 min⁻¹, whereas TiO₂-AC exhibited the highest k of 0.0422 min⁻¹, which indicates its enhanced dye degradation capability. The degradation results show clearly that the photodegradation of MO improved in the presence of AC in the core of the TiO₂ NSs. AC has a well-developed pore structure, large surface area, and strong adsorption capacity. In the composite, AC acts as a center at which the organic pollutant molecules are adsorbed and concentrated before they are transferred to the illuminated TiO₂ NSs for degradation, which results in high rates of reaction and in turn, high rates of MO degradation. The increased absorption of light also resulted in the production of more electron–hole pairs, which helps to enhance the degradation rate. The long-term stability of the composite material is of high importance for applications, hence the degradation activity of TiO₂-AC was examined in three successive MO degradation reactions. The MO solution with a concentration of 0.03 mM was degraded in 60 min, and the performance

was consistent over the three cycles, which indicates a stable catalytic activity for TiO₂-AC (Figure 5b).

Besides MO, the samples were also investigated in the degradation of VOCs, namely, ethanol, methanol, and formaldehyde (which can exist as indoor air pollutants; Figure 5c and Figure S8). Before illumination, the samples were left in the dark for 120 min to attain an adsorption–desorption equilibrium between the composite material and the VOC vapor (Figure S7). Upon illumination with UV light, the TiO₂-AC composite was able to degrade photocatalytically all three VOCs completely in the shortest time amongst the samples tested. Similar to the MO degradation results, the excellent performance can be attributed to the adsorption properties of the AC core as it has a high surface area and abundant active adsorption sites and aids in the adsorption and concentration of the VOC vapors, which are then degraded photocatalytically by the TiO₂ NSs. The degradation kinetics is shown in Figure S8, and the pseudo-first-order rate constants k of the various photocatalysts are summarized in Table S2. The TiO₂-AC composite has a higher k than A-TiO₂ and TiO₂ NSs for all the VOCs tested. The repeatability of the TiO₂-AC composite was also tested in repeated degradation of ethanol vapor with a concentration of 300 ppm (Figure 5d). Consistently, TiO₂-AC could degrade ethanol to completion in 30 min over the three cycles of testing. This shows that the composite material is stable over prolonged and repeated use in the photodegradation of VOCs.

Conclusions

Carbon nanospheres derived from a hydrothermally treated glucose solution were transformed successfully into thin-layered planar sheets and hierarchical pores with a high specific surface area through a cost- and process-effective process of simultaneous activation–exfoliation–reassembly. The materials

possess a hierarchical porous structure that consists of micro-/meso-/macropores. TiO₂ nanosheets were then grown on the hierarchical porous carbon structure as a proof-of-concept demonstration of a composite material that facilitates the efficient transport of reactants throughout the carbonaceous matrix, which leads to the enhanced adsorption and photocatalytic degradation performance of aqueous and gaseous organic pollutant compounds. This monolithically integrated, dual-functionality material system could possibly serve as a promising sustainable environmental remediation solution in the future.

Experimental Section

Synthesis of CSs and KOH activation

D-(+)-Glucose (1.89 g; Sigma Aldrich) was dissolved in deionized (DI) water (35 mL) and placed in a 50 mL Teflon-lined stainless-steel autoclave at 190 °C for 4 h. After it was cooled to RT, the brown mixture was collected and washed three times using DI water by centrifuging. The precipitate was then dried at 80 °C for 6 h, and the brown solid obtained was CSs. The CSs were then subjected to KOH (Acros Organics) activation treatment with CS/KOH mass ratios of 1:2, 1:4, and 1:6 and labeled as AC-1, AC-2, and AC-3, respectively. CSs (0.1 g) were mixed with the corresponding amount of KOH in an agate mortar and pestle and subsequently annealed under flowing N₂ at 600 °C for 2 h with a ramping rate of 20 °C min⁻¹. The resultant product was washed repeatedly with DI water until the pH reached 7 and then dried at 70 °C for 5 h.

MO adsorption by AC

AC (5 mg) was dispersed in aqueous MO solution (10 mL, 0.24 mM) by sonication, and the mixture was stirred magnetically in the dark. At regular time intervals of 15 min, the mixture was centrifuged, extracted, and passed through a 0.2 μm syringe filter (Thermo Scientific), before we analyzed the concentration of the MO solution by using a UV/Vis/NIR spectrophotometer. The maximum absorbance peak value at λ = 462.5 nm was used to plot the amount of MO adsorbed and, thus, to determine the adsorption activity of the AC.

VOC adsorption by AC

AC (1 mg) was coated onto a 1.5 × 2.5 cm glass substrate that was then placed into a quartz vial reactor. The reactor was filled with a VOC/Ar vapor mixture (2000 ppm). The VOCs tested were ethanol, methanol, and formaldehyde. Gas samples of 100 μL were extracted at regular time intervals with a gas-tight syringe and injected into a GC-MS system (Shimadzu GCMS-QP2010 Ultra) to determine the concentration of VOC that remained in the reactor.

Synthesis of TiO₂-AC

AC (5 mg) was dispersed in pure ethanol (20 mL, Merck) by ultrasonication for 5 min. Titanium tetraisopropoxide (TTIP; 40 μL; Sigma Aldrich) was added to the solution, and the mixture was stirred for 5 min, followed by the addition of diethylenetetramine (DETA; 200 μL; Alfa Aesar) and 10 min of stirring. The solution was heated at 200 °C for 20 h in a Teflon-lined stainless-steel autoclave. Once cooled, the product was washed with ethanol by centrifug-

ing several times and dried at 80 °C. Finally, the dried product was annealed at 450 °C for 2 h with a heating rate of 2 °C min⁻¹. This composite material is denoted as TiO₂-AC.

Photocatalytic degradation of aqueous MO

The powdered photocatalyst (10 mg) was dispersed in aqueous MO solution (20 mL, 0.06 mM) in a quartz vial reactor by sonication. The mixture was then stirred magnetically in the dark for 60 min to achieve a complete adsorption-desorption equilibrium before irradiation by using a 160 mW light emitting diode (LED) of wavelength 365 nm. The concentration of MO was determined by using a UV/Vis/NIR spectrophotometer, and the maximum absorbance peak value at λ = 462.5 nm was used to plot the amount of MO degraded and, thus, to determine the photodegradation activity of the TiO₂-AC composite.

Photocatalytic degradation of VOCs

The powdered photocatalyst (1 mg) was coated on a 1.5 × 2.5 cm glass substrate that was then placed into a quartz vial reactor. The reactor was filled with VOC vapor of 2000 ppm concentration. The VOCs tested were ethanol, methanol, and formaldehyde. The mixture was left in the dark for 2 h to achieve a complete adsorption-desorption equilibrium before it was illuminated by using a 160 mW LED of wavelength 365 nm. Gas samples (100 μL) were extracted at regular time intervals with a gas-tight syringe and injected into a GC-MS system (Shimadzu GCMS-QP2010 Ultra) to determine the concentration of VOC that remained in the reactor.

Materials characterization

The morphology of the nanostructures was characterized by using SEM (JEOL FEG JSM 7001F) operated at 15 kV. The elements present in the nanostructures were analyzed by using EDX (Oxford Instruments) and scanning transmission electron microscopy (STEM; JEOL 2100 TEM). The crystalline structures of the TiO₂-AC composite were analyzed by using XRD (D5005 Bruker X-ray diffractometer equipped with graphite-monochromated CuK_α radiation at λ = 1.541 Å) and TEM (JEOL 2100 TEM). BET (Quantachrome Nova 2200e) measurements were conducted with N₂ as the adsorbate at 77 K. The specific surface area (S_{BET}) was calculated according to the multiple-point BET method at P/P₀ = 0.01–0.1. Porosity distributions were calculated by the QSDFT and Barrett–Joyner–Halenda (BJH) method. The total pore volume was obtained from the volume of N₂ adsorbed at P/P₀ ≈ 0.99. Absorption spectra of the samples were measured by using a UV/Vis/NIR spectrophotometer (Shimadzu UV-3600). FTIR spectra of the products were recorded by using a Shimadzu IRPrestige-21 FTIR spectrophotometer. The concentration of VOCs was measured by using GC-MS (Shimadzu GCMS-QP2010 Ultra).

Acknowledgements

This research is supported by the National Research Foundation (NRF), under Energy Innovation Research Programme (EIRP) R-263-000-B82-279, managed on behalf of the Building and Construction Authority (BCA).

Conflict of interest

The authors declare no conflict of interest.

Keywords: adsorption · carbon · layered materials · mesoporous materials · nanostructures

- [1] A. K. Geim, K. S. Novoselov, *Nat. Mater.* **2007**, *6*, 183–191.
- [2] S. L. Candelaria, Y. Shao, W. Zhou, X. Li, J. Xiao, J.-G. Zhang, Y. Wang, J. Liu, J. Li, G. Cao, *Nano Energy* **2012**, *1*, 195–220.
- [3] E. Lam, J. H. T. Luong, *ACS Catal.* **2014**, *4*, 3393–3410.
- [4] P. Hadi, J. Guo, J. Barford, G. McKay, *Environ. Sci. Technol.* **2016**, *50*, 5041–5049.
- [5] R. Mas-Ballesté, C. Gomez-Navarro, J. Gomez-Herrero, F. Zamora, *Nanoscale* **2011**, *3*, 20–30.
- [6] M. Yi, Z. Shen, *J. Mater. Chem. A* **2015**, *3*, 11700–11715.
- [7] K. R. Paton, E. Varrla, C. Backes, R. J. Smith, U. Khan, A. O'Neill, C. Boland, M. Lotya, O. M. Istrate, P. King, T. Higgins, S. Barwich, P. May, P. Puczkarski, I. Ahmed, M. Moebius, H. Pettersson, E. Long, J. Coelho, S. E. O'Brien, E. K. McGuire, B. M. Sanchez, G. S. Duesberg, N. McEvoy, T. J. Pennycook, C. Downing, A. Crossley, V. Nicolosi, J. N. Coleman, *Nat. Mater.* **2014**, *13*, 624–630.
- [8] Y. Zhang, L. Zhang, C. Zhou, *Acc. Chem. Res.* **2013**, *46*, 2329–2339.
- [9] L. Mao, Y. Zhang, Y. Hu, K. H. Ho, Q. Ke, H. Liu, Z. Hu, D. Zhao, J. Wang, *RSC Adv.* **2015**, *5*, 9307–9313.
- [10] L. Xu, L. Guo, G. Hu, J. Chen, X. Hu, S. Wang, W. Dai, M. Fan, *RSC Adv.* **2015**, *5*, 37964–37969.
- [11] D. Lozano-Castelló, M. A. Lillo-Ródenas, D. Cazorla-Amorós, A. Linares-Solano, *Carbon* **2001**, *39*, 741–749.
- [12] M. Sevilla, A. B. Fuertes, *Chem. Eur. J.* **2009**, *15*, 4195–4203.
- [13] X. Sun, Y. Li, *Angew. Chem. Int. Ed.* **2004**, *43*, 597–601; *Angew. Chem.* **2004**, *116*, 607–611.
- [14] Y. Guo, S. Yang, K. Yu, J. Zhao, Z. Wang, H. Xu, *Mater. Chem. Phys.* **2002**, *74*, 320–323.
- [15] X. Zheng, W. Lv, Y. Tao, J. Shao, C. Zhang, D. Liu, J. Luo, D.-W. Wang, Q.-H. Yang, *Chem. Mater.* **2014**, *26*, 6896–6903.
- [16] J. Wang, S. Kaskel, *J. Mater. Chem.* **2012**, *22*, 23710–23725.
- [17] X. Zheng, J. Luo, W. Lv, D.-W. Wang, Q.-H. Yang, *Adv. Mater.* **2015**, *27*, 5388–5395.
- [18] B. Gao, P. S. Yap, T. M. Lim, T.-T. Lim, *Chem. Eng. J.* **2011**, *171*, 1098–1107.
- [19] S. Helali, E. Puzenat, N. Perol, M.-J. Safi, C. Guillard, *Appl. Catal. A* **2011**, *402*, 201–207.
- [20] A. A. Vega, G. E. Imoberdorf, M. Mohseni, *Appl. Catal. A* **2011**, *405*, 120–128.

Manuscript received: January 18, 2017

Revised manuscript received: February 27, 2017

Accepted manuscript online: March 2, 2017

Version of record online: May 22, 2017
